

## Ultra High Energy Cosmic Rays: Techniques and Results\*

---

**Antonella Castellina<sup>†</sup>**

*IFSI-Istituto Nazionale di Astrofisica, Torino, Italy*

*E-mail: [castellina@to.infn.it](mailto:castellina@to.infn.it)*

**Wara Chamani**

*Carrera de Física, Universidad Mayor de San Andrés, La Paz-Bolivia*

*E-mail: [nosferatum\\_777@yahoo.es](mailto:nosferatum_777@yahoo.es)*

The experimental techniques and the most important astrophysical problems in the Ultra High Energy region (UHE) above  $\sim 10^{17}$  eV are briefly reviewed. After a general introduction about the sources and propagation of ultra high energy cosmic rays, we review the experimental detection techniques starting with a short historical overview. The most recent results on the UHE cosmic ray spectrum and composition are discussed, with particular emphasis on those from the HiRes and Pierre Auger Observatory. We finish with a short overview of the future experiments aiming at the study of the energy region above  $10^{17}$  eV.

*4th School on Cosmic Rays and Astrophysics,*

*August 25- September 04, 2010*

*Sao Paulo Brazil*

---

\*This article is based on a series of lectures given at the "Fourth School on Cosmic Rays and Astrophysics", August 25 to September 4, 2010, Sao Paulo - Brasil

<sup>†</sup>Speaker.

## 1. Introduction

A large contribution to the knowledge and understanding of the Galaxy is given by the observation of the most energetic particles, the cosmic rays (CRs). These relativistic particles, reaching the Earth from the outer space, are either primary nuclei, arriving directly from the sources, or secondary products of the spallation processes (i.e. fragmentation by nuclear destruction) taking place during the propagation from the sources through the interstellar medium (ISM).

Cosmic rays play an important role in the dynamics of the Galaxy: their energy density  $\rho_E \simeq 1 \text{ eV/cm}^3$  is comparable to the energy density of the visible starlight  $\rho_S \simeq 0.3 \text{ eV/cm}^3$ , the galactic magnetic fields  $B^2/2\mu_0 \simeq 0.25 \text{ eV/cm}^3$  (if  $B \simeq 3\mu\text{G}$ ) or the cosmic microwave background (CMB) radiation  $\rho_{CMB} \simeq 0.25 \text{ eV/cm}^3$ . Such non thermal component is strictly linked to radiation and magnetic fields. The challenge we are facing is that of identifying the sources of cosmic rays and the mechanism through which low energy particles are accelerated to such high energy to be called cosmic rays and of understanding their propagation through the galactic magnetic fields.

The cosmic ray all-particle energy spectrum at Earth can be described as a power law  $J(E) = k E^{-\gamma}$ . It is shown in Fig.1, multiplied by  $E^{2.5} \text{ eV}$  to highlight the characteristic changes of slope known as the *knee*, at 3-5 PeV and the *ankle*, around 4 EeV and the drop in the flux above few  $10^{19} \text{ eV}^1$ . The study of these features brings information on the mechanisms of production and acceleration of cosmic rays. Due to the wide energy range and the rapidly changing flux, it is obvious that different experimental techniques are needed in diverse energy regions. Direct measurements of the primary cosmic rays can be performed up to  $10^{14} \text{ eV}$ . Above this threshold, the low fluxes due to the steeply falling spectrum force us to exploit indirect methods, detecting the extensive air showers generated by the interaction of cosmic rays in the atmosphere. In the figure, the total and center of mass energies corresponding to the current accelerators are also shown. The cosmic ray extreme energies are by far beyond the reach of the most powerful man-made accelerators, so that they are of great interest also from the point of view of particle physics, probing the standard models of hadronic interactions and the laws of relativity in extreme domains.

## 2. Sources and Propagation

Based on the first theory of cosmic ray acceleration developed by Fermi [1], the most accredited mechanism to convert from the kinetic motion of the plasma to kinetic energy of charged particles is the diffusive acceleration in presence of shock waves (DSA) powered by supernovae explosions propagating from the remnant to the interstellar medium [2]. Traversing the boundary between the unshocked upstream and the shocked downstream region back and forth, charged particles gain each time an energy <sup>2</sup>  $\Delta E \propto E$ . The acceleration spectrum follows a power-law in momentum,  $Q(E) \propto p^{-\alpha}$ , with  $\alpha$  located between 2.0 and 2.5. Taking into account the diffusion of cosmic rays in the Galaxy, with a diffusion coefficient  $K$  expected to be proportional to the rigidity of the particle ( $R = pc/Ze$ , where  $Z$  is the charge and  $c$  is the speed of light) as  $K \propto R^\delta$ , this will eventually lead to the observed spectrum at Earth  $N_{obs}(E) \propto E^{-\gamma}$ , with  $\gamma = \alpha + \delta$ , up to a maximum

<sup>1</sup>Energies are often given in units of TeV, PeV, EeV, corresponding to  $10^{12}, 10^{15}, 10^{18} \text{ eV}$  respectively.

<sup>2</sup>For relativistic shocks,  $\Delta E \propto \Gamma E$ , where  $\Gamma$  is the Lorentz factor.

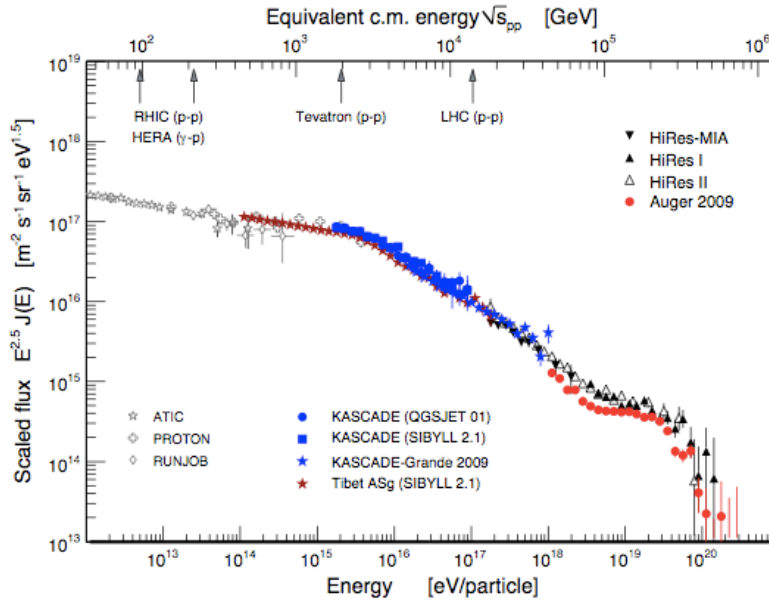


**Figure 1:** All-particle energy spectrum of cosmic rays. The corresponding center-of-mass energies for the past and current accelerators are also shown.

energy

$$E_{max} \simeq Ze(B/\mu G)(L/pc)\beta_{shock} \text{ PeV} \quad (2.1)$$

where  $Ze$  is the particle charge,  $B$  is the galactic magnetic field strength,  $L$  is the linear dimension of the acceleration site and  $\beta_{shock}$  is the shock velocity. The maximum energy for the acceleration is thus proportional to the particle charge. As an example, an updated version of the original *Hillas plot* is shown in Fig.2 [3]. Different potential sources are indicated, among which gamma ray bursts (GRB), powerful radiogalaxies (RG) and blazars (BL): only those above the thick line have the right configurations of  $B$  and  $L$  to accelerate protons up to  $10^{20}$  eV<sup>3</sup>.

At ultra high energies, cosmic rays must be extragalactic. The Larmor radius of a charged particle ( $E, Z$ ) in a magnetic field  $B$  is in fact  $r_L = E_{PeV}/B_{\mu G}Z$ ; at 1 EeV, for a typical Galactic magnetic field of  $2 \div 3 \mu G$ , it exceeds the dimension of our galaxy (which radius is  $\sim 15$  kpc and which disk is  $\sim 200$  pc thick). In this energy range, the cosmic ray trajectory is deflected from the original source direction, on average, as  $\theta(E) \simeq 2.7^\circ \left( \frac{60 \text{ EeV}}{E/Z} \right) \int_0^D \frac{dx}{\text{kpc}} \times \frac{B}{3 \mu G}$ .

The relation between the CR number density  $u_{CR}$  and the flux  $\Phi$  is

$$\Phi \left( \frac{\text{part}}{\text{cm}^2 \text{s sr}} \right) = \frac{u_{CR} \beta c}{4\pi} \quad (2.2)$$

from which one can derive the energy density<sup>4</sup>

$$u_{CR} = \frac{4\pi}{\beta c} \int E \frac{d\Phi}{dE} dE = \frac{4\pi}{\beta c} \int E^2 \frac{d\Phi}{dE} d \ln E \quad (2.3)$$

<sup>3</sup>A similar plot can be constructed for iron: in this case, acceleration to  $10^{20}$  eV is also possible in low-power active galaxies (e.g. Seyfert galaxies).

<sup>4</sup>Due to the very steeply falling energy spectrum, it is useful to write the integral in  $\ln E$  to obtain the area under a semilogarithmic plot of the integrand proportional to the integral itself.

Following [4], the emissivity ( $\text{erg}/(\text{Mpc}^3 \text{ yr})$ ), that is the energy density of CRs divided by the energy loss mean time, needed to power UHECRs can be calculated by making the simple assumption that they are all protons (we do not know the actual composition) that suffer energy loss due to universe expansion, photopion and pair production on CMB photons and taking as their intensity the one measured by the Pierre Auger Collaboration [5].

Using energies in units of  $10^{20}$  eV and intensity in units of  $10^{24}$  to simplify the notation, we get after few calculations and change of units the emissivity:

$$\varepsilon = \frac{6 \cdot 10^{45}}{L_{\text{Loss}}[\text{Mpc}]} \frac{J_{24}}{E_{20}} \frac{\text{erg}}{\text{Mpc}^3 \text{ yr}} \quad (2.4)$$

Using the appropriate loss lengths obtained from propagation calculations one finds, for example, that a source able to accelerate protons to  $10^{20}$  eV would need an emissivity of  $0.4 \cdot 10^{-44} \text{ erg}/(\text{Mpc}^3 \text{ yr})$ .

Examples of sources with these kind of emissivities are

- Active Galactic Nuclei (AGN): central regions of galaxies displaying energetic phenomena which cannot be attributed to stars. In the most powerful ones, e.g., a region about  $10^4$  times smaller than the host galaxy can be about  $10^4$  times brighter than the whole galaxy. At first order, different orientations of the source with respect to the line of sight explain different phenomenologies.
- Gamma Ray Bursts (GRB): long duration GRBs result from the core collapse of massive stars, giving rise to a black hole and an accretion disk and, at the end of the outflow expansion, to two highly relativistic jets. Both internal and external shocks in the jets are supposed to be able to accelerate baryons to ultra high energies. Recent results from the Fermi experiment [6] suggest that iron nuclei are more likely to be accelerated in AGN rather than protons, while both of them could be brought to  $\geq 10^{20}$  eV in the most powerful GRBs.

In contrast with the conventional *bottom-up* models just described, *top-down* models have been introduced in the past to circumvent the problem of accelerating particles to ultra high energies. According to them, UHE cosmic rays are not accelerated from low to ultra high energies in the sources, but on the contrary they are produced in the decay of supermassive relic particles [7]. They were also supposed to explain the absence of the GZK cutoff suggested in the past by the AGASA experiment. However, as we will see below, the experimental observation of the cutoff and the limits obtained about the fraction of primary photons seem to rule out most of these models.

Due to the expansion of the Universe, particles which come from sources at redshift  $z$  lose their energy as  $E \rightarrow E/(1+z)$ . The attenuation length is  $c/H_0 \simeq 4000 \text{ Mpc}$  (for a Hubble constant  $H_0 = 75 \text{ km s}^{-1} \text{ Mpc}^{-1}$ ).

During their travel from the source to the Earth, nuclei interact with the radiation fields permeating the intergalactic space, and these interactions produce visible features in the measured CR spectrum [8]. For a background photon energy  $\varepsilon$  (typically  $\varepsilon_{\text{CMB}} \simeq 10^{-3}$  eV), protons can lose energy by two main mechanisms:

(i) pair production ( $p + \gamma_{\text{CMB}} \rightarrow p + e^+ + e^-$ ), acting as catalyzers to convert a photon into a pair. The energy threshold is

$$E_{\text{thr}} = \frac{(m_N + m_e)m_e}{\varepsilon} \simeq \frac{5 \cdot 10^{14}}{\varepsilon} \text{ eV} \quad (2.5)$$

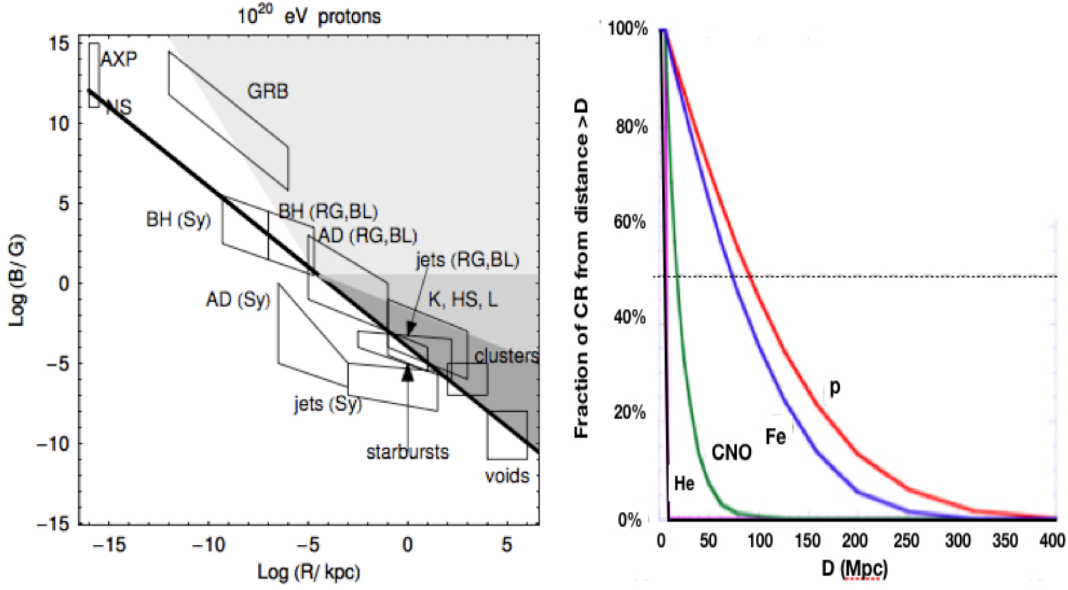


**Figure 2:** Example of constraints on sources: only those above the thick line can accelerate protons to  $10^{20}$  eV ([3] and refs. therein).

**Figure 3:** Fraction of cosmic rays with energy  $6 \cdot 10^{19}$  eV coming from a distance  $> D$  as a function of  $D$  [Mpc]. 50% is indicated by the dashed line.

while the proton attenuation length is  $> 1000$  Mpc.

(ii) pion photoproduction ( $p + \gamma_{CMB} \rightarrow p[n] + \pi^0[\pi^+]$ ) has a threshold of

$$E_{thr} = \frac{(m_N + m_\pi/2)m_\pi}{\epsilon} \simeq \frac{7 \cdot 10^{16}}{\epsilon} \text{ eV} \quad (2.6)$$

The proton attenuation length  $O(100)$  Mpc (the well known Greisen-Zatsepin-Kuzmin (GZK) "horizon" [9]). Since the inelasticity for pair production interactions  $k = m_{sec}/m_N \simeq 0.001$  is very low compared to that for the pion production  $k \simeq 0.15$ , the energy loss due to the first one is much less significant than that due to the second. Apart from dense regions in the Universe, like the center of Galaxies, the other energy loss processes are negligible.

Neutrons can be created in the interactions of the protons near the sources or in the photoproduction reactions, then disintegrate through  $\beta$  decay ( $n \rightarrow p e^- \bar{\nu}_e$ ) which is the dominant energy loss process below  $10^{20}$  eV. The rate of neutron decay is  $\Gamma_n = m_N/\tau_n E$ , where  $\tau_n \simeq 886$  sec is the mean lifetime of the neutron. The propagation range reaches up to 1 Mpc at  $10^{20}$  eV:

$$R_n = \tau_n \frac{E}{m_N} \simeq 0.9 \left( \frac{E}{10^{20} \text{ eV}} \right) \text{ Mpc} \quad (2.7)$$

As a consequence, we should in principle be able to observe a source of neutrons from the center of the Galaxy, since at 1 EeV their propagation range would be about 10 kpc (8 kpc is in fact our distance from the Galactic centre).

The most important energy loss for heavier nuclei is that due to photodisintegration: a photon is absorbed, generating first an unstable state and then the emission of one or more nucleons (when the photon energy is higher than the binding energy of nucleons inside the nucleus). The minimum

loss length will be much shorter than that of protons, but at a factor  $A$  higher energy. For high energies, most nucleons are ejected. The pair production in the field of the nucleon is taking place also for heavy nuclei, but the energy loss is proportionally greater by a factor  $Z^2/A$  and the loss length is  $Z \times 20$  EeV.

In Fig.3, the fraction of CRs arriving on Earth from a given distance is shown for different nuclei, from protons to iron, with energy  $E = 6 \cdot 10^{19}$  eV. Most intermediate nuclei disintegrate during propagation, leaving basically only protons and iron nuclei.

### 3. Techniques to study UHECRs

Primary cosmic rays above  $\simeq 10^{14}$  eV are characterized by a very low flux, which goes from few  $10^{-19}$  to about  $10^{-35} \text{ m}^{-2}\text{s}^{-1}\text{sr}^{-1}\text{eV}^{-1}$  between  $10^{14}$  eV and  $10^{20}$  eV and their energy, mass and arrival directions can be studied only indirectly by exploiting the particle cascades that they produce in the atmosphere. The measured observables are the longitudinal and lateral distributions of the charged components or the Cherenkov and the fluorescence light produced during the propagation of the extensive air shower (EAS) in the Earth atmosphere down to the experimental level. Since all observables are interrelated and depend in different ways on both energy and mass of the primaries, multiparametric measurements are to be preferred: modern experimental setups in fact include detectors of many shower components.

When a primary cosmic ray nucleus interacts with an air nucleus in the upper atmosphere, a leading nucleon emerges, while a fraction (the so-called inelasticity  $k$ ) of its initial energy goes into production of secondaries<sup>5</sup>, mainly  $\pi$  mesons; due to charge independence, the energy is equally shared among  $\pi^+$ ,  $\pi^-$  and  $\pi^0$ .

The electromagnetic component ( $e^+$ ,  $e^-$  and photons) originates from the fast decay of neutral pions into photons, which initiates a rapid multiplication of particles in the shower, mainly through two production processes: bremsstrahlung by electrons and pair production by photons. The multiplication continues until the rate of energy loss by bremsstrahlung equals that of ionization, at a critical energy which in air is  $E_c \simeq 86$  MeV. The hadronic back-bone of the shower continuously feeds the electromagnetic part; the charged pions can either interact or decay. The nucleon interaction length in air (where  $\langle A \rangle \simeq 14.5$ ) is <sup>6</sup>  $\simeq 80 \text{ g cm}^{-2}$ . The transverse momentum of nucleons and pions and the multiple scattering of the shower particles, particularly of the electrons, are responsible for the lateral spread of the particles in the shower. Finally, charged pions decay into muons (and neutrinos). Since muons lose energy mainly through ionization and excitation, they are not attenuated very much and give rise to the most penetrating component of the shower.

The classical air shower experiment consists of an array of detectors, either scintillator counters or water Cherenkov tanks, distributed over a wide area, which surface is chosen depending on the rate of events to be studied. The separation between the detectors is tuned to match the scale of the shower footprint at the observation level (tens of meters in the PeV region, hundreds of m to km for the arrays studying the extreme energy region). At each location, the particle density of one or more charged components is measured with detectors of size suitable for the component

<sup>5</sup>the definition of "secondaries" applies here to cosmic rays produced in the Earth atmosphere, not to be confused with the secondary particles originating from the spallation of primary cosmic rays in the interstellar medium.

<sup>6</sup>Depths in an absorber are usually measured in units of  $x = h \times \rho$ , that is in  $[cm] \times [g/cm^3] = [g/cm^2]$

under study (few  $m^2$  for the electromagnetic one, much larger for muons and hadrons), together with the arrival times of the particles and their time spread. Due to the large number of secondary particles, the active area to be covered can be much smaller than the total one: for example, the sensitive/enclosed area ratio can go from  $\simeq 3 \cdot 10^{-3}$  for the EAS-TOP array [10] ( $37 \times 10 \text{ m}^2$  detectors over  $10^5 \text{ m}^2$ ) to  $\simeq 5 \cdot 10^{-6}$  for the Pierre Auger Observatory [11] ( $1600 \times 10 \text{ m}^2$  detectors over  $3000 \text{ km}^2$ ). This ratio, together with the altitude of the detector (that is thickness of the atmosphere above it) and the ability to detect different components of an EAS, determines the energy thresholds of different detectors.

The more penetrating muon component is generally measured by shielded detectors, like scintillator slabs: a shielding of thickness some radiation lengths can absorb the electromagnetic component without significantly affecting the muon one. Alternatively, one can use tracking devices (limited streamer or proportional tubes) or measure the muons, together with the electromagnetic component, in water Cherenkov tanks. In this last case, the electromagnetic particles are completely absorbed in water, while the muon signal is proportional to the track length in the detector. Since low energy muons (below 1 GeV) mainly decay before reaching the ground, this component basically consists of muons with energies of few GeV. High energy muons, with energies above few TeV, on the other hand, give information on the first interactions of the primary particle. They can be detected in underground laboratories, shielded by rock, water or ice [12, 13], either as single muons or bundles.

Charged particles of the air shower produce Cherenkov light if their velocity is such that  $v/c > n$ , where  $n(h)$  is the index of refraction as a function of height  $h$ . The broader lateral distribution of the Cherenkov light, due to the smaller absorption of photons in atmosphere, and the high photon density, that means a better signal-to-noise ratio even for smaller arrays, are the main advantages in using this kind of detectors. The Cherenkov light emitted by the shower particles in the atmosphere can be studied by two different techniques:

- (i) Light integrating detectors combine a large angular acceptance with the advantages of Cherenkov light detection. They are used to measure the lateral distribution of the Cherenkov light with a grid of photomultipliers distributed over a large area on the ground.
- (ii) Imaging Detectors are used to reconstruct air showers exploiting the production in the focal plane of an image corresponding to the intensity pattern and direction of Cherenkov light.

The charged secondary particles of the air showers can also excite nitrogen molecules in the atmosphere: their de-excitation results in the isotropic emission of a fluorescence light with spectrum in the near UV region (300-400 nm). The fluorescence yield is the number of fluorescence photons emitted per unit of energy deposited in the atmosphere, and it amounts to  $\simeq 4 \div 6$  photons/MeV. In clear moonless nights the fluorescence light can be collected with mirrors and projected onto a camera generally made of a large number of photomultiplier tubes (PMTs), which record a time sequence of light. The PMTs are pointing in different directions so to cover a large field of view. The shower appears as a trace of illuminated PMTs (pixels). As simulations show, most of the total energy of the shower is detectable as ionization energy, but a correction must be introduced to take into account the fraction of energy not contributing to the total signal (carried by muons and neutrinos).

### 3.1 Past and present experiments

The history of UHE cosmic ray experiments started as early as the 1940's [14]. The technique of fast timing for shower reconstruction was first developed in the Agassiz experiment from M.I.T., but only in the sixties the first event with an estimated energy above  $10^{20}$  eV was detected in Volcano Ranch. A larger array of water Cherenkov tanks built in Haverah Park was used to exploit for the first time the particle density at a large distance from the core as an energy estimator. A more complex array was that of Yakutsk, where surface and underground detectors were used together and the first calorimetric evaluation of the shower energy was determined by using an array of 35 photomultipliers exploiting the Air Cherenkov technique. AGASA, in Japan, was then the first real "giant" array; from its data came the suggestion of a primary spectrum extending above  $10^{20}$  eV, pointing to the absence of the GZK cutoff.

The idea of exploiting the fluorescence light was first proposed by K.Greisen in the Cornell experiment, but only few years later, with the use of Fresnel lenses in the Tokyo experiment, the first light was actually seen. Pioneering work on the atmospheric monitoring needed to disentangle the background from the EAS fluorescence was performed by the Fly's Eye group, which also first employed a stereoscopic system. The HiRes experiment was built based on the experience gained with Fly's Eye. Its two units of mirrors (21 and 42 for the two sites) separated by 12.6 km can cover ( $3^\circ - 16.5^\circ$ ) and ( $3^\circ - 30^\circ$ ) respectively in elevation above the horizon and  $360^\circ$  in azimuth.

While surface detectors have a 100% duty cycle, the fluorescence ones can work only in clear moonless nights, thus reaching  $\simeq 10\%$  duty cycle. The big advantage in the latter is that of observing the longitudinal development of showers as far as 25-30 km, making a quasi calorimetric measurement of their energy.

The advantages of the two techniques are now exploited together in the Pierre Auger Observatory, which design consists in fact of both a surface detector (SD) and a fluorescence detector (FD). The SD [11] is an array of over 1600 surface detectors arranged on a triangular grid with 1.5 km spacing. This  $3000 \text{ km}^2$  array is overlooked by 24 fluorescence telescopes grouped by 6 at four locations on its boundary, forming the FD [15].

The hybrid technique (see Fig.4(a)), combining data recorded by both the SD and the FD detectors ("hybrid" sample), has great advantages: (a) the energy scale is set with the fluorescence telescopes and is thus nearly independent of shower simulations; (b) the shower arrival directions are determined with very high precision, cross-checking the SD angular resolution; (c) the two techniques are complementary and different observables are measured in a redundant way and many cross-checks are possible. An example showing the energy deposit in atmosphere by a EAS as reconstructed in the Pierre Auger fluorescence detector is shown in Fig.4(b).

Table 1 and table 2 list the past and present surface and fluorescence detectors investigating the UHE cosmic rays.

### 3.2 Reconstruction of EAS

#### 3.2.1 Surface Detectors

The reconstruction of EAS parameters in surface detectors is based on the measure of the number of secondary particles crossing the counters as a function of time, thus sampling the shower at one atmospheric level (the experimental site level).

Experiment	Site	Operation [yr]	Array	Area [km <sup>2</sup> ]
Agassiz	Massachusetts	1956	plastic scintillators	~ 0.7
Volcano Ranch	New Mexico	1957-63	19 plastic scintillators	~ 8
INS-LAS	Japan	1968	22 plastic scintillators 20 m <sup>2</sup> spark chamber 19 $\mu$ detectors	~ 0.8
Haverah Park	UK	1967-87	62 water tanks	~ 12
Yakutsk	Siberia	1969-95	58 scintillators 6 $\mu$ detectors 35 Cherenkov detectors	~ 18
SUGAR	Australia	1968-79	54 $\mu$ detectors	~ 60
AGASA	Japan	1990-2004	111 scintillators 29 $\mu$ detectors	100
Pierre Auger	Argentina	2002-now	1600 water tanks	3000
Telescope Array	Utah	2007-now	507 scintillators	700

**Table 1:** Past and present surface shower detectors investigating the UHE region.

Experiment	Site	Operation [yr]	Array	Location
Cornell	USA	1964-67	Fresnel lens	3 sites (11,16,12 km)
INS-Tokyo	Japan	1968	Fresnel lens	
Fly's Eye	Utah	1981-93	FE-I: 67 mirrors FE-II: 36 mirrors	2 sites 3.4 km apart
HiRes	Utah	1994-2004	HR-I: 21 mirrors HR-II: 42 mirrors	2 sites 12.6 km apart
Pierre Auger	Argentina	2002-now	24 mirrors	4 sites around the SA
Telescope Array	Utah	2007-now	38 mirrors	3 sites around the SA

**Table 2:** Past and present fluorescence detectors investigating the UHE region.

The arrival direction of the primary particle is derived from the measure of the arrival time of particles on the stations (the shower front) and from the position of the counters, on an event by event basis. Most detectors in the UHE range have time resolution from 1° to 3°, a precision good enough if compared to the expected deflection of the particle directions due to the Galactic magnetic fields.

The core location and the total number of charged particles are obtained by means of a fit to a function describing their measured lateral distribution. Many different functional forms have been used in the past to describe the lateral distribution, generally modified Nishimura-Kamata-Greisen formulas like

$$S(r) = \left( \frac{r}{r_{opt}} \right)^\beta \left( \frac{r + r_{700}}{r_{opt} + r_{700}} \right)^{\beta+\gamma} \quad (3.1)$$

where  $r_{opt}$  is a characteristic distance at which the fluctuations in the lateral distribution are minimized and which value depends basically only on the geometry of the apparatus. The chosen

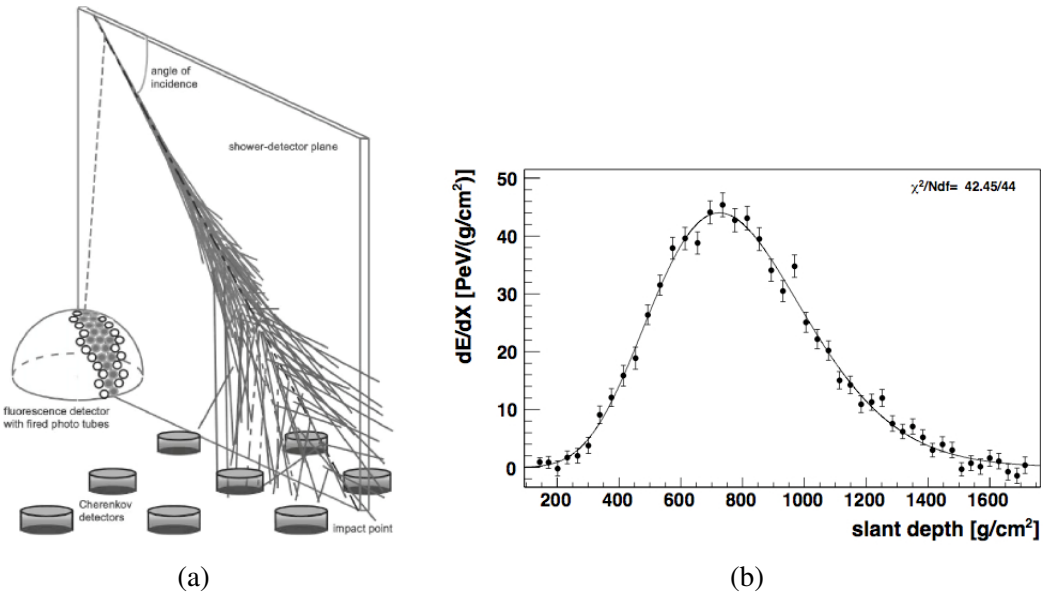


**Figure 4:** (a) Sketch of a hybrid detector. (b) The reconstructed energy deposit profile for an EAS in the Pierre Auger fluorescence detector. Reconstructed energy  $(3.0 \pm 0.2) 10^{19}$  eV [15].

function must take into account the increasing muon-to-electromagnetic ratio at large core distances, where the electromagnetic component has been strongly absorbed and what is seen is the flatter muon lateral distribution function.

Energy is obtained by measuring the particle density at  $r_{opt}$ , evaluating it at a reference angle  $\theta_{ref}$  after correcting for the attenuation of showers in the atmosphere (EAS arriving at large zenith angle have a longer path in atmosphere and are thus more attenuated). Based on simulations,  $S(r_{opt}, \theta_{ref})$  can finally be related to the primary energy:  $E = kS(r_{opt}, \theta_{ref})^\beta$ .

Ground arrays cannot measure directly the primary mass. The most sensitive observable is the muon number, which can be measured by means of dedicated counters buried underground. In limited and favourable conditions, that is not too close to the shower core and at large angles, with detectors able to record the temporal distribution of the particles with good sampling, one can hope to count muons by counting the muon peaks in the traces, or by measuring the time evolution of the early part of the distribution, which is dominated by muons.

### 3.2.2 Fluorescence Detectors

The fluorescence light is seen by the PMTs as a time sequence of triggered pixels. The shower geometry can be obtained by finding the shower-detector plane, that is the plane including the telescope location and the axis defined by the time sequence of illuminated pixels (see Fig.5). The distance of closest approach  $R_p$ , the time  $t_0$  along the shower axis at  $R_p$  and the angle  $\chi_0$  between the ground plane and the shower axis are obtained by minimizing

$$t_i = t_0 + \frac{R_p}{c} \tan\left(\frac{\chi_0 - \chi_i}{2}\right) \quad (3.2)$$

where  $t_i$  is the time at which light reaches the  $i$ -th PMT. The geometrical resolution improves significantly (to fraction of degree for the shower axis determination) either using a second telescope (stereo mode) or having an independent measure of the time of arrival of the shower to the ground (e.g. using a surface detector).



**Figure 5:** Geometry reconstruction for a fluorescence telescope ([16]).

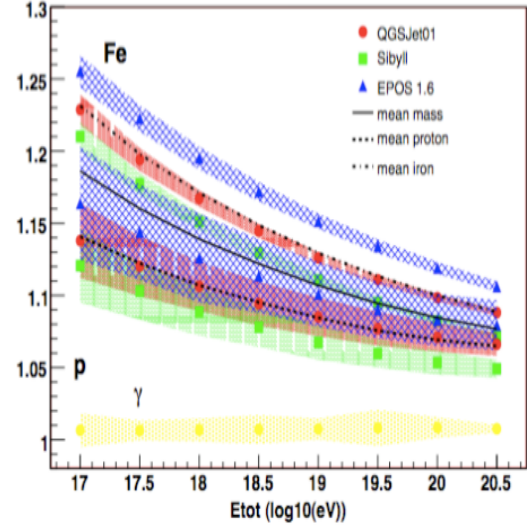


**Figure 6:** Missing energy correction in the energy evaluation from FD [17].

The total electromagnetic energy released in the atmosphere by the EAS is proportional to the integral of the longitudinal development of the EAS, which can be described by a Gaisser-Hillas function [18]

$$N_e(X) = N_e^{max} \left( \frac{X - X_0}{X_{max} - X_0} \right)^{(X_{max} - X_0)/\lambda} \exp \left( - \frac{X_{max} - X}{\lambda} \right) \quad (3.3)$$

The primary energy can then be obtained by correcting for the missing energy, that is the energy transported by undetected muons and neutrinos, which parametrization according to simulations is shown in Fig.6. The correction depends on the primary energy and mass and on the hadronic interaction model used in the simulations. It amounts to  $\simeq 20(10)\%$  for iron (proton) at  $10^{18}$  eV (using QGSJet), but it decreases with increasing energy, because at higher energy the pions mostly interact producing  $\pi^0$ s, which go to feed the EM component (the one measured) instead of decaying into muons, which get lost.

A direct measure of the depth of shower maximum  $X_{max}$  allows to derive information about the primary mass, although only on statistical bases due to the intrinsic fluctuations of the observable. Both the  $X_{max}$  and the width of its distribution are strictly related to the primary mass.

In the case of hybrid experiments, with both surface and fluorescence detectors, good quality hybrid data can be used to define the energy scale: the signal  $S(r_{opt})$  detected by means of the SD at large distance from the core can be correlated to the energy  $E_{FD}$  directly measured by the FD, thus deriving directly the relation  $E_{FD} = k \times S(r_{opt})^\alpha$  for the sample of hybrid events.

The energy scale can then be applied to calibrate the full sample of events from the Surface Detector, for which one can exploit the huge statistics and the well known exposure.

#### 4. The energy spectrum

The primary energy spectrum above  $10^{17}$  eV, as measured by the different experiments, is shown in Fig.7 multiplied by a factor  $E^3$  to better show the deviations from a pure power law [20]. The ankle, that is a change of slope in the energy region characterizing the transition from Galactic to extragalactic cosmic rays, is clearly seen. Fitting the spectrum with different power laws  $J_i = k E_i^{-\gamma}$  in different energy regions  $\Delta E_i$ , the HiRes and Pierre Auger groups find the slope and energy values indicated in the first three lines of Table 3; their results are plotted together in Fig.8.

The presence of the GZK cutoff above few  $10^{19}$  V was questioned by the AGASA result in the past [21], giving rise to a wealth of so-called "top-down" models for the production of the UHE particles. More recently, the existence of a suppression in the flux of UHECRs has been firmly established by HiRes [22] and Pierre Auger [5], compatible with that expected for the GZK cutoff. The slopes before and after the cut-off and the corresponding energy according to HiRes and Pierre Auger are shown in the last three lines of Table 3. The depletion could also be attributed to the reach of maximum energy of the sources; this possibility could be ruled out if the anisotropy onset at the same energy of the GZK threshold is confirmed.

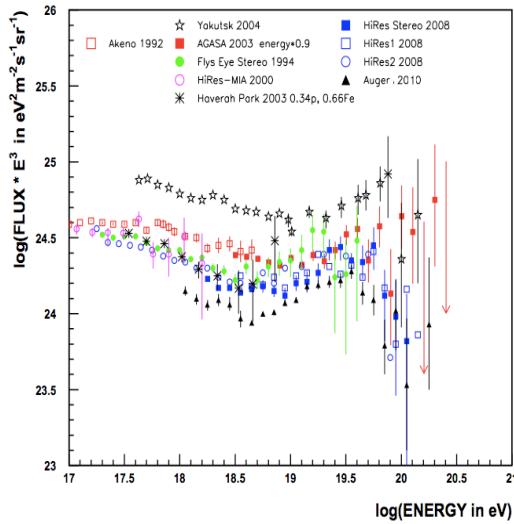


**Figure 7:** Primary energy spectrum in the transition region and above [20].

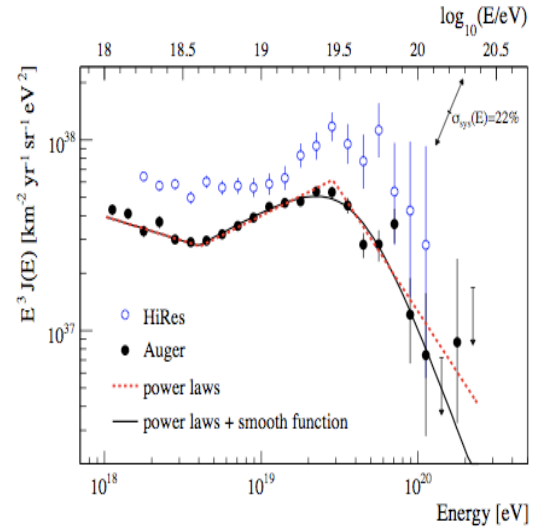


**Figure 8:** Primary energy spectrum as measured by the Pierre Auger and HiRes experiments [23].

The systematic uncertainties play a leading role here: they are entangled with the statistical ones in the spectrum representation of the figure (due to the  $E^3$  multiplication), but it can be shown that a good agreement both in the flux normalization and in the ankle position can be reached if they are properly taken into account.

The systematic errors are different for different detectors:

(i) Surface Detectors : they depend mainly on the single particle definition and its calibration, on the shower reconstruction, on the sensitivity of different detectors to different particles, on the dynamic range covered by detectors and finally on the simulation codes and embedded hadronic interaction models used to derive the energy.

(i) Fluorescence Detectors : they are due to the single photon calibration, shower reconstruction,

	HiRes	HiRes	Pierre Auger
	Mono	Stereo	Hybrid+SD
Slope ( $E < E_{ankle}$ )	$3.25 \pm 0.01$	$3.31 \pm 0.11$	$3.26 \pm 0.04$
$\log_{10}(E_{ankle})$	$18.65 \pm 0.05$	$18.56 \pm 0.06$	$18.61 \pm 0.01$
Slope ( $E \geq E_{ankle}$ )	$2.81 \pm 0.03$	$2.74 \pm 0.05$	$2.59 \pm 0.02$
$\log_{10}(E_{GZK})$	$19.75 \pm 0.04$	$19.76 \pm 0.11$	$19.46 \pm 0.03$
Slope ( $E \geq E_{GZK}$ )	$5.1 \pm 0.7$	$5.5 \pm 1.8$	$4.3 \pm 0.2$

**Table 3:** Summary of slope spectrum results of HiRes and Pierre Auger Observatory.

atmospheric corrections and to the fluorescence yield, which is presently the main source of systematic uncertainties [26]. Many different experiments have been brought on to measure it: the results span from  $\simeq 4$  to  $\simeq 6$  photons/MeV.

The shape of the spectrum depends on the calculation of the aperture. For a surface detector, it is given by the effective area integrated over solid angle. This area coincides with the geometrical one at full efficiency, i.e. when the acceptance does not depend on the nature of the primary particle, its energy or arrival direction. For Pierre Auger, this happens above 3 EeV, where the calculation of the exposure is purely geometrical, being the integration of the geometrical aperture over the observation time. In the case of HiRes, on the contrary, the aperture is rapidly growing with energy, since at higher energy the showers are brighter and can thus be detected at larger distances. It is determined by simulations, and it saturates above 100 EeV.

The overall systematic uncertainty on the energy scale is  $\simeq 17\%$  for HiRes. In the Pierre Auger Observatory, the uncertainty in the evaluation of the energy scale amounts to  $\simeq 22\%$ .

## 5. The mass composition

The knowledge of the mass composition of the primary beam is of the utmost importance for any study on origin, acceleration, propagation of the UHE cosmic rays. In fact, all different models of acceleration depend on the particle type. From a more technical point of view, also the methods employed by surface and fluorescence detectors to obtain the energy spectrum of the primaries depend on their mass. The aperture of surface detectors and the correction for the missing energy for fluorescence detectors, for example, vary depending on the primary mass.

Our knowledge of the composition of primary cosmic rays in the transition region and above is quite poor. The mass can be measured only indirectly and only on statistical basis, because of the fluctuations in the first interaction point and development of the showers. The conclusions reached by the different groups depend on the methods used to measure the mass and, most important, they are dependent, to a greater or lesser extent, upon the interaction model that is assumed in the simulations needed to interpret the data.

The depth of maximum development of the extensive air showers,  $X_{max}$ , is the key observable to study the mass composition of the primary cosmic rays. Its variation per decade of primary energy, the so-called 'elongation rate', is sensitive to changes in the nature of the primary and less dependent on the hadronic interaction models compared to the shower maximum itself. Furthermore, the shower to shower fluctuations in  $X_{max}$  are expected to decrease for heavier primary nuclei and

increase with the nuclear interaction length. It should be stressed, however, that while  $X_{max}$  can be directly measured by fluorescence detectors (with precisions of 30-40 g/cm<sup>2</sup>), the interpretation of the results in terms of average primary mass strongly depends on the hadronic interaction model used in the simulations. The most recent results on  $X_{max}$  and the width of its distribution from Pierre Auger [24] and HiRes [25] are shown in Fig.9.

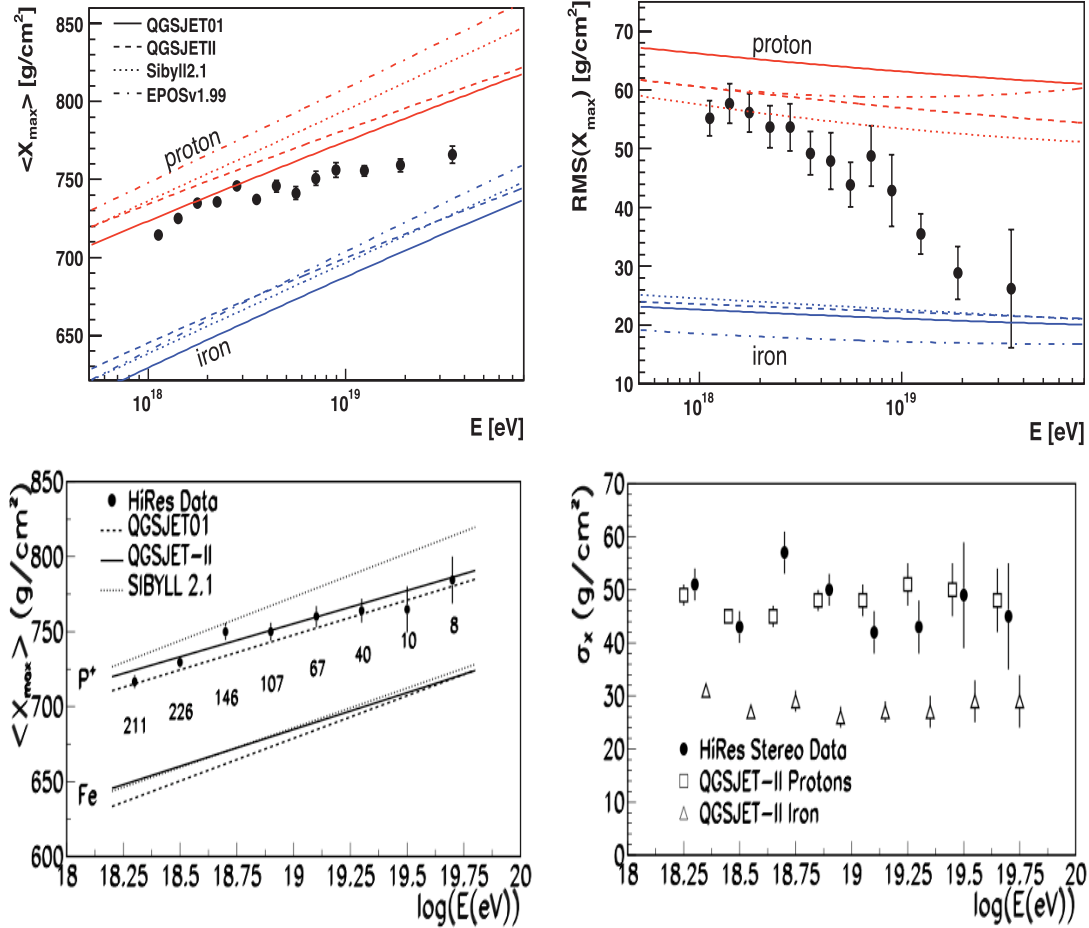


**Figure 9:** The dependence of  $X_{max}$  (left panel) and of its fluctuations (right panel) on the primary energy in comparison with the predictions of different hadronic interaction models from Pierre Auger [24] (top panels) and HiRes [25] (bottom ones).

The HiRes result suggests a predominantly proton composition (at least with QGSJet hadronic interaction models) and an almost constant composition across the ankle. On the other hand, according to Pierre Auger data, the measured change in elongation rate can be interpreted in two ways: either the primary composition is getting heavier at the highest energies or there must be a significant change in hadronic interaction properties in this energy range.

The comparison between the two results is however not simple: the different data selection criteria and the different definitions of  $X_{max}$  and RMS could eventually explain the disagreement.

Composition studies can also be performed making use of observables measured by surface detectors. One can e.g. exploit the fact that different particles in the air shower arrive to the ob-

servation level with different time spread, due to geometrical effects, differences in the particle velocities, multiple scattering, geomagnetic deflections. In fact, muons dominate the earlier part of the signal, since they arrive earlier and over a period of time shorter than the electromagnetic particles (em). The risetime of the signals in the detectors and the azimuthal features of the time distributions can be related to the depth of shower maximum, and are thus sensitive to the primary composition. As recently shown by the Pierre Auger group [27], the results obtained with these more indirect methods are consistent with those found using the fluorescence detector.

According to the superposition model <sup>7</sup>, a shower produced by an iron nucleus will contain a larger fraction of muons (more than 80%) at the observation level than a shower of the same energy created by a proton primary. Muons have been widely used to study composition in the lower energy region around 1 PeV, but unfortunately they are only about 10% of the total particles in a shower, so that the use of muon detectors in giant arrays becomes unaffordable. Muon density measurements have been carried on in the past in the AGASA experiment [28]. Their data seem to suggest a proton dominated composition above 10 EeV, but these kind of measurements are dominated by large fluctuations and the conclusion is very sensitive to the hadronic interaction model included in the simulations used to interpret the data.

The muon number can also be obtained by exploiting the universality properties of showers.

In fact, thanks to the huge amount of particles in an extensive air shower at UHE, the shower properties are statistically smoothed and EAS can be characterized by only three parameters: the primary energy, the depth of shower maximum and the overall normalization of the muon component. With the possibility of using the hybrid events, the Pierre Auger Collaboration measured the muon number relative to that expected from simulation by exploiting the shower universality properties. Denoting the electromagnetic signal by  $S_{EM}$  and the muon signal by  $S_{\mu}$ , which evolution with shower age is universal, one can write

$$S_{MC}(E, \theta, \langle X_{max} \rangle) = S_{EM}(E, \theta, \Delta X) + N_{\mu}^{rel} S_{\mu}(QGSJet - II, p, 10EeV) \quad (5.1)$$

where  $N_{\mu}^{rel}$  is defined as the number of muons relative to that of QGSJET-II proton showers at 10 EeV. Since  $\langle X_{max} \rangle$  is known from FD measurements, the only unknown is here  $N_{\mu}^{rel}$ , which can be measured at a reference energy (10 EeV).

One of the key observables to distinguish among model predictions on the origin of the highest energy cosmic rays is the fraction of primary cosmic ray photons. They can be produced in standard GZK processes (from the  $\pi^0$  decay) or in exotic scenarios like those predicted by top-down models (see [29] and refs. therein). Showers from photon primaries have larger  $X_{max}$  (deeper in atmosphere) compared to hadronic ones: the multiplicity in electromagnetic interactions is in fact maller, so that more generations are needed to degrade the energy to the critical value.

Above 10 EeV, they are subject to the LPM effect, which results in a suppression of the pair production and bremsstrahlung cross sections and an increase of shower fluctuations (4 times those of iron showers at 10 EeV, 1/3 more than those of protons) and contain fewer secondary muons, because the mean free path for muon from photonuclear interactions and muon pair production is

<sup>7</sup>The superposition model states that an EAS from a primary (E,A) can be considered as the superposition of A nucleon showers, each with energy E/A.

more than 2 orders of magnitude higher as compared to the radiation length <sup>8</sup>.

From the experimental point of view, photons can be recognized through their peculiar longitudinal development (deep shower maximum) by the FD. The SD provides other two observables: the rise time of the signal in the stations at a given distance from the core (which is increased in case of the deep developing photon primaries) and the radius of curvature of the shower front (which is smaller in case of the deep developing photon primaries due to geometrical reasons).

The upper limits on the fraction of photons are shown in Fig.10(left). The most recent ones, obtained with the Pierre Auger Observatory data [29], rule out many top-down models. The expected GZK photon fluxes are well below the current bounds, but could be reached in the near future.

Astrophysical neutrinos are expected to be produced in GZK interactions from the decay of charged pions; being undeflected by magnetic fields, they bring information on the sources and unveil hidden regions of the Universe. Neutrinos are produced at different abundances, but their oscillations during propagation leads to equal numbers of the three flavours. From the experimental point of view, neutrino showers can be tagged as those produced deep in atmosphere (a deep neutrino interaction in air, or a  $\tau$  decay) showing a large electromagnetic component on surface detectors at ground, characterized by a broad signal in time (young showers). In fact, nuclear showers are on the contrary produced higher up, and reach the ground as a thin and flat front of muons, while the electromagnetic component has been almost completely absorbed (old showers). Fig.10 (right) displays the most recent limits on the cosmogenic neutrinos. Different approaches are based on the Askaryan charge excess in UHE neutrino induced showers within Antarctic ice [31]

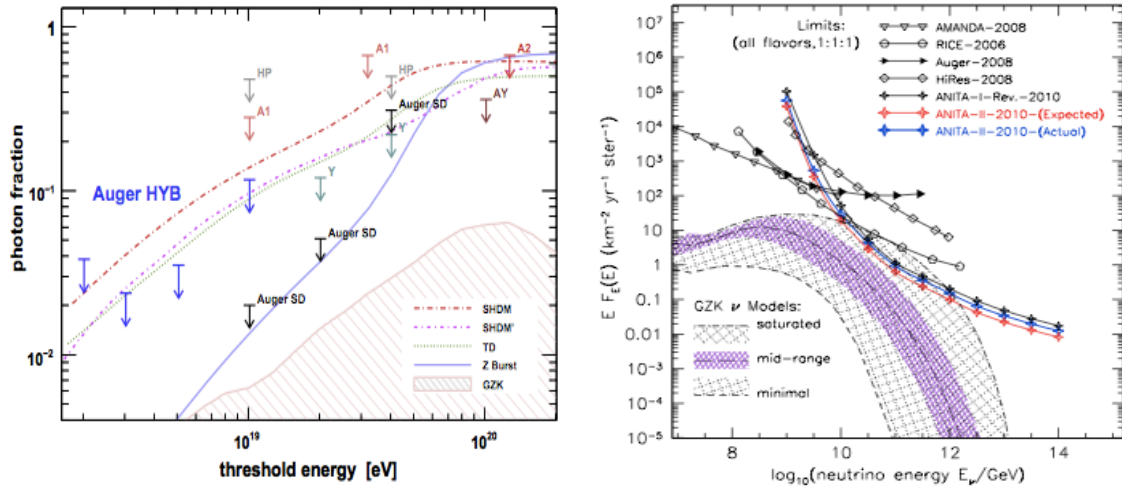


**Figure 10:** Left panel: limits on the photon fraction in cosmic rays as a function of energy [29]. Right panel: compilation of existent limits on the neutrino flux ([30] and refs therein).

## 5.1 The astrophysical interpretation

The simplest and most natural way of producing a flattening (an ankle) in the cosmic ray spectrum is that of intersecting the steep galactic spectrum with a flatter extragalactic one. This

<sup>8</sup>An opposite effect is that of pre-showering: above 50 EeV photons can convert in the geomagnetic field (giving an e+e- pair) and create a preshower before entering the Earth atmosphere. This makes the  $X_{max}$  and its fluctuations smaller (higher up) because the EAS observed is the superposition of many EAS from lower energy em particles

is the basic idea behind the *ankle model* [32]: the transition from galactic to extragalactic cosmic rays appears around  $10^{19}$  eV, at the crossing of the two spectra, producing also the observed "dip", a concavity in the spectrum at  $10^{18} \lesssim E \lesssim 4 \cdot 10^{19}$  eV. If this model is correct, then additional mechanisms able to accelerate the galactic component to such high transition energy have to be introduced.

In the *dip model* [33], the dip is supposed to be produced by the  $e^+e^-$  pair production in the interactions between extragalactic protons (after their escape from the sources) and CMB photons. The transition takes place at the energy at which the adiabatic energy losses due to the expansion of the Universe equal the pair production ones, that is around the so-called second knee ( $E \simeq 5 \cdot 10^{17}$  eV). The model requires an almost pure proton composition, with a maximum allowed contamination from He of  $\simeq 10\%$ .

The *mixed composition model* [34] assumes that the extragalactic cosmic ray source composition is mixed and similar to that of the galactic cosmic rays. The transition region covers energies up to the ankle, while the galactic component extends up to more than  $10^{18}$  eV. A possible difficulty of the mixed model is the fact that the single element spectra cut off at energies proportional to their mass  $A$ . The composition could be dominated by protons below  $10^{18}$  eV, unlike in the ankle model case.

Energy spectrum, composition and anisotropy are used to discriminate among the different models. The first one is the best measured but, as shown in Fig. 11 for the dip and mixed composition cases, all models give a quite good description of the all-particle energy spectrum.

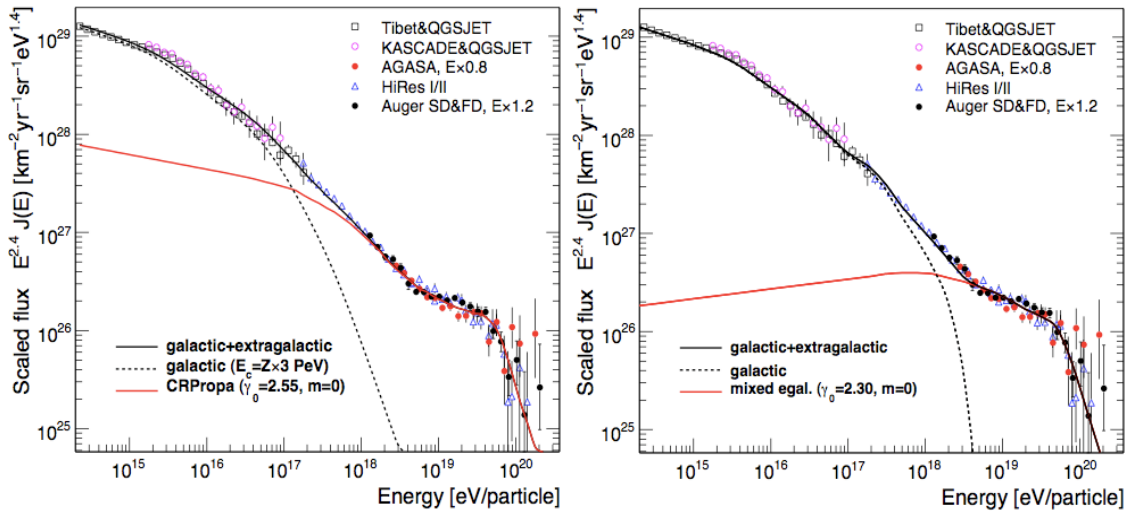


**Figure 11:** The measured all-particle flux compared to the dip and mixed models described in the text [35].

The study of composition seems to be more efficient in discriminating among the different hypotheses. According to the dip model, the  $\langle X_{max} \rangle$  evolution with energy is steep till the transition ends, becoming then flatter and corresponding to extragalactic protons. In the mixed model, the transition is wider and the evolution of  $\langle X_{max} \rangle$  less steep, going from the heavy galactic part to the mixed but light extragalactic composition. As of today, however, none of the three models can

satisfactorily reproduce all the data. In the case of the mixed composition, the higher number of free parameters allows an easier adjustment.

From the experimental point of view, we need to understand the disagreement between the results on composition from HiRes and Pierre Auger. The first can be explained by a quite simple model, in which cosmic rays above 1 EeV are protons for extragalactic origin and the UHE spectrum is shaped by their interactions with the cosmic microwave background, while such a simple picture does not fit the Pierre Auger data. A serious comparison of the results taking into account the differences in the selection of events, definition of depth of shower maximum and its fluctuations and systematic uncertainties is mandatory. Furthermore, the interpretation of the results is strongly dependent on both the composition and the knowledge of the hadronic interaction properties in the UHE range. Only in the case in which these properties can be extrapolated to the ultra high energy range (where no data from accelerators will be available even in the future) one will be able to draw conclusion about the cosmic ray composition.

Another possible key to explore the transition region is that of cosmogenic neutrinos. The neutrino fluxes depend on the source density evolution, CR composition and maximum energy of the accelerated cosmic rays. They can be calculated for different model parameters, distinguishing for the source distribution the two cases of uniform and star formation rate strong evolution, for the composition the pure proton and mixed ones and different values for  $\beta$  and  $E_{max}$ . According to [36], high  $E_{max}$  and strong evolution with redshift of the sources would be preferred in case of neutrino detection by Auger or Anita. If, as recently shown [37], these scenarios are excluded by Fermi/LAT results on the diffuse extragalactic gamma ray background [38], the detection of these UHE neutrinos would require an increase of at least a factor  $\simeq 10$  in the current experiments sensitivity.

## 6. The future

The investigation of the region above the knee towards the transition to extragalactic cosmic rays requires detectors with large areas but with smaller spacing compared to the arrays studying UHE cosmic rays. As for the lower knee region, the requirement is that of employing complementary techniques, so to detect as many components of showers as possible and cross check their systematics. Numerous new projects have been designed and are now taking data or are under construction. Among them, Cascade-Grande [39], Tunka-133 [40] and Ice-Top [41] aim at exploring the end of the galactic spectrum, eventually detecting the iron knee.

In the Pierre Auger Observatory site, two enhancements are under construction: AMIGA [42], an infill of tanks with 750 m spacing plus buried muon detectors, and HEAT [43], which employs three fluorescence telescopes able to look at lower energy shower. They will study the transition region from  $10^{17}$  up to  $10^{19}$  eV and give us more information about the composition up to 1 EeV. As for the highest energy region, the continuous operation of the Pierre Auger Observatory and the data taken by the Telescope Array [44] in the Northern hemisphere, started in 2009, will allow to shed more light into the UHE region.

The Telescope Array detector will cover a surface of  $\sim 700 \text{ km}^2$  with 507 scintillator counters overlooked by three fluorescence detectors. Note that the two hybrid experiments are placed in the

Southern (Pierre Auger) and Northern (Telescope Array) hemisphere; the full sky coverage is of great importance in the anisotropy measurements [45].

An engineering array of radio detection stations (AERA), which will investigate the radio emission of showers in the UHE region [46], is also being deployed in the Pierre Auger site .

A much larger statistics in the UHE region, above 60 EeV, could be obtained building the northern site of the Pierre Auger Observatory [47] in Colorado. The design calls for 4000 water tanks covering 20000 km<sup>2</sup> in a  $\sqrt{2}$  miles grid, plus 39 fluorescence telescopes, but the construction has unfortunately been postponed in the USA to some time in the future.

### Acknowledgements

One of the authors (A.C.) wishes to thank the organizers of the 4th School on Cosmic Rays and Astrophysics for their invitation to give this series of Lectures and for their warm hospitality, and Prof.Saavedra for his advices. Many thanks also go to the students for their interest, questions and discussions.

### References

- [1] E. Fermi, Phys.Rev. **75** (1949) 1169.
- [2] E. Berezhko, JETP **89** (1999) 391.
- [3] K.V. Ptitsyna and S.V. Troitsky, Phys. Usp. **53** (2010) 691.
- [4] C. Dermer, Invited Talk at the 30th Int. Cosmic Ray Conf., Merida, Mexico (2007); arXiv:0711.2804v2.
- [5] J.Abraham et al. (Pierre Auger Coll.), Phys.Rev.Lett. **101** (2008), 061101 [<http://www.auger.org/>]
- [6] C. Dermer and S. Razzaque, Astrop.J., **724** (2010) 1366.
- [7] V. Berezhinsky, V., Nucl. Phys. B (Proc.Suppl.) **70** (1999) 419.
- [8] P.Bhattacharjee, Phys.Rep.**327** (2000) 109.
- [9] K.Greisen,Phys.Rev.Lett. **16** (1966) 748; G.T.Zatsepin and V.A.Kuzmin, JETP Lett. **4** (1966) 78.
- [10] M. Aglietta et al. (EAS-TOP Coll.), Nucl. Instrum. Meth. A, **277** (1989) 23.
- [11] J.Abraham et al. (Pierre Auger Coll.), Nucl.Instr. Meth. in Phys. Res. A **523** (2004), 50.
- [12] M. Ahlen et al. (MACRO Coll.), Nucl.Instr.Methods A **324** (1993) 337.
- [13] A. Achterberg et al. (IceCube Coll.), Astrop.Phys. **26** (2006) 155 [<http://icecube.wisc.edu/>]
- [14] M.Nagano, J.Phys.Soc.Jpn **70** (2001) Suppl.B, 1.
- [15] J.Abraham et al. (Pierre Auger Coll.), Nucl.Instr. Meth. in Phys. Res. **A620** (2010) 227.
- [16] D.Kuempel et al., Astrop.Phys. **30** (2008) 167.
- [17] T. Pierog, Proc. of the 30th Int. Cosmic Ray Conf., Merida, Mexico (2007).
- [18] T.Gaisser and M.Hillas, Proc. of the 15th Int. Cosmic Ray Conf., Plovdiv (Bulgaria) **8** (1977) 353.
- [19] C. Di Giulio (Pierre Auger Coll.), Proc.31th Int.Cosmic Ray Conf., Lodz, Poland (2009); arXiv:0906.2189.

- [20] M.Nagano, *New J.Phys.* **11** (2009) 065012.
- [21] M.Takeda et al. (AGASA Coll.), *Phys.Rev.Lett.* **81** (1998) 1163  
[<http://www-akeno.icrr.u-tokyo.ac.jp/AGASA/>]
- [22] R.U.Abbasi et al. (HiRes Coll.),*Phys.Rev.Lett.* **100** (2008) 101101. [<http://www.cosmic-ray.org/>]
- [23] J. Abraham et al. (Pierre Auger Coll.), *Phys. Lett. B* **685** (2010) 239.
- [24] J. Abraham et al. (Pierre Auger Coll.), *Phys.Rev.Lett.* **104** (2010) 91101.
- [25] R.U.Abbasi et al. (HiRes Coll.),*Phys.Rev.Lett.* **104** (2010) 161101.
- [26] F.Arqueros et al., *New J. Phys.* **11** (2009) 065011.
- [27] H. Wallberg (Pierre Auger Coll.), *Proc.31th Int.Cosmic Ray Conf., Lodz, Poland (2009);*  
arXiv0906.2319.
- [28] K.Shinozaki (AGASA Coll.), *Nucl.Phys.B Proc.Suppl.* **151** (2006) 3.
- [29] J.Abraham et al. (Pierre Auger Coll.), *Astrop.Phys.* **31**, 6 (2009) 399.
- [30] J. Abraham et al. (Pierre Auger Coll.) **79** (2009) 102001.
- [31] P.W.Gorham et al. (ANITA Coll.), *Phys.Rev.D* **82** (2010) 022004  
[<http://www.phys.hawaii.edu/anita/web/index.htm>]
- [32] M. Hillas, *J.Phys.G* **R95** (2005) J31.
- [33] V.Berezinsky, *Phys.Rev.D* **74** (2006) 043005.
- [34] D.Allard et al., *Astrop.Phys.* **27** (2007) 61.
- [35] M.Unger, arXiv:0812.2763.
- [36] D.Allard, arXiv:0906.3156v1.
- [37] V.Berezinsky et al.,arXiv:1003.1496 (2010).
- [38] A.A.Abdoet al. (Fermi/LAT Coll.), arXiv:1002.3603, (2010).
- [39] W. Ape et al. (KASCADE-Grande Coll.), *Nucl.Instr. and Meth.Phys.Res.A* **620** (2010) 202.
- [40] N.M.Budnev et al. (TUNKA Coll.), 30th Int.Cosmic Ray Conf., Merida, Mexico (2007);  
arXiv:0801.3037 [<http://www.inr.troitsk.ru/eng/intcol/tunkae.html>]
- [41] S. Klepser et al. (Ice-Top Coll.), *Proc.ECRS* (2008) [<http://www.bartol.udel.edu/icetop/>]
- [42] M.Platino (Pierre Auger Coll.), *Proc.31th Int.Cosmic Ray Conf., Lodz, Poland (2009);*  
arXiv0906.2354.
- [43] M.Kleifges (Pierre Auger Coll.), *Proc.31th Int.Cosmic Ray Conf., Lodz, Poland (2009);*  
arXiv0906.2354.
- [44] H.Tokuno et al. (TA Coll.),*AIP Conf.Proc.* **1238** (2010) 365 [<http://www.telescopearray.org/>]
- [45] S. Mollerach, these Proceedings (2010).
- [46] A.M.van den Berg et al. (Pierre Auger Coll.), *Proc.31th Int.Cosmic Ray Conf., Lodz, Poland (2009);*  
arXiv0908.4422. [[http://www.augerradio.org/wiki/moin.cgi/Public Information](http://www.augerradio.org/wiki/moin.cgi/Public%20Information)]
- [47] J.Blumer et al. (Pierre Auger Coll.), *New J.Phys.* **12** (2010) 035001.